Selective autophagy of ribosomes balances a tradeoff between starvation survival and growth resumption

Authors

Joel Tuomaala[1,2], Devanarayanan Siva Sankar[3], Julie Perey[1], Sacha Psalmon[1,2], Nicholas Stroustrup[4], Joern Dengjel[3], Benjamin D. Towbin[1,*]

Affiliations

[1] Institute of Cell Biology, University of Bern; Bern, Switzerland.

[2] Graduate School for Cellular and Biomedical Sciences, University of Bern; Bern, Switzerland.

[3] Department of Biology, University of Fribourg; Fribourg 1700, Switzerland.

[4] Centre for Genomic Regulation (CRG), The Barcelona Institute of Science and Technology (BIST).

*corresponding author (benjamin.towbin@unibe.ch)

Abstract

In environments with fluctuating nutrient abundance, organisms must survive periods of starvation, yet quickly resume growth upon food encounter. A tradeoff between these objectives is well-documented in microbes, where it is caused by the need to partition the total cellular protein content between growth- and survival-enhancing proteins. However, the molecular mechanisms of growth-survival tradeoffs in multicellular animals remain largely unknown. Here, we addressed this mechanism for *C. elegans* by measuring the dynamic changes of its proteome during starvation using live imaging and proteomics. We found that starved animals catabolize ribosomal proteins through autophagy, which provides essential energy for survival while preserving organismal integrity. However, the resulting decline in ribosomes delayed growth resumption upon refeeding until pre-starvation ribosome levels were restored. Genetic inhibition of ribosomal autophagy had a dual effect: although it accelerated growth after short starvation, it compromised survival during prolonged starvation. These findings reveal the rate of ribosomal catabolism as a key determinant of a tradeoff between starvation survival and rapid growth resumption whose tuning may adapt animals to different starvation durations. Our research shows how the need to balance protein allocation between growth and survival constrains animal physiology, highlighting the mechanistic role of proteome resource limitation in whole-organism tradeoffs.

Introduction

In nature, organisms face alternating periods of food abundance and scarcity. They must therefore effectively withstand times of starvation and rapidly resume growth when food becomes available. This dual requirement necessitates a delicate balance between investing in growth and survival [1–3].

Tradeoffs between growth and survival have been extensively characterized in microorganisms [4,5], where they are primarily governed by the partitioning of a limited proteome between growth-promoting and survival-enhancing functions [6–10]. In microbes, the growth rate follows a simple linear relation with the ribosome content called the 'growth law' [11,12]. Thus, while high expression of survival factors improves survival under starvation, it also sequesters resources from the production of ribosomes that would be needed for maximal growth [7].

Growth-survival tradeoffs are also prevalent in multicellular animals [2,13], but their underlying cellular and molecular mechanisms remain poorly understood. Do the molecular constraints of proteome partitioning [14] also explain tradeoffs occurring in animals? Or is a more nuanced and comprehensive mechanistic analysis required to understand tradeoffs in these much more complex multicellular systems? Addressing these questions can identify universal principles of organismal tradeoffs and reveal fundamental design principles of biological systems.

During starvation, eukaryotes catabolize their protein content by autophagy [15,16]. While autophagy supports survival by providing vital energy and metabolites, it can also harm survival by degrading essential cellular components [17]. In principle, this threat could be mitigated by the selective degradation of proteins that are not needed during starvation, such as ribosomes, which remain largely idle during starvation-induced growth arrest. Indeed, selective autophagy of ribosomes, called ribophagy, occurs in amino acid-starved yeast [18]. However, whether starvation also induces ribophagy in other eukaryotes and if ribophagy has a physiological role for the starvation resistance of animals remains contentious [19–24].

To resolve this controversy and explore the role of protein resource allocation in tradeoffs at a multicellular scale, we used the nematode *C. elegans* as the model system. The natural habitat of *C. elegans* is characterized by boom-bust cycles of rapid population growth and extended starvation [15,25]. An appropriate balance between survival and growth resumption is thus central to its fitness in the wild, and its genetic tractability make it well-suited to address the mechanisms involved.

Here, we monitored the dynamic changes of the proteome during starvation and refeeding of *C. elegans* larvae by proteomics and live imaging techniques. Our measurements showed unambiguously that starvation induces selective ribophagy, leading to a progressive decline in the ribosome levels. This decline in ribosomes delayed resumption of growth upon refeeding until the pre-starvation ribosome concentrations were restored. Reminiscent of microbial growth laws, the speed of growth resumption was near-linearly related to the ribosome levels at the start of refeeding, which suggests that linear growth laws also inform on physiological tradeoffs in complex multicellular animals. Indeed, by genetically manipulating the rate of ribophagy, we could predictably alter the balance between growth and survival and show that preserving ribosomes accelerates growth resumption but impairs survival during prolonged starvation.

Together, our findings reveal the rate and selectivity of ribophagy as key determinants in balancing starvation survival and growth resumption in a multicellular animal. This discovery highlights that the partitioning of limited proteome resources plays a key mechanistic role in tradeoffs at an organismal scale,

bridging the gap between microbial and multicellular biology in the molecular understanding of fundamental tradeoffs.

Results

Ribosomal proteins decline rapidly during starvation

To measure proteome dynamics during starvation, we conducted quantitative label-free proteomics [26] of L1 larvae of *C. elegans* after 1, 4, and 9 days of starvation (Fig. 1a). Using suitable algorithms to compare relative amounts of different proteins within the same sample (iBAQ [27]) and relative changes of individual proteins across different samples (LFQ [28]), we detected 2624 and 1787 proteins consistently across all conditions and repeats. Ribosomes contributed 12.1% (s.e.m. = 0.2%) to the total detected protein mass, as estimated by iBAQ, on day 1 of starvation and dropped by 27% (s.e.m. = 1.3%) to 9.0% (s.e.m. = 0.3%) by day 9 of starvation. Non-ribosomal cytoplasmic proteins declined by only 12.5% (s.e.m. = 1.7%), whereas nuclear and filamentous or membrane bound proteins increased in their relative abundance (Fig. 1d). Consistent with previous reports [29], the total mitochondrial protein mass also declined rapidly (-23.8%, s.e.m. = 3.0%). Notably, our experiments measured protein abundance relative to the total protein mass and not the absolute protein amount per animal. The observed decline in ribosomal proteins is thus not a byproduct of an overall size reduction or protein loss and shows that ribosomal proteins decline more rapidly than the total proteome. An increase in relative protein abundance, as observed for nuclear proteins (Fig. 1d-e), may be due to *de novo* synthesis of these proteins or due to a net decline that was slower than that of the total proteome.

Comparisons of the relative changes of individual proteins over time, estimated by LFQ, confirmed these conclusions. Ribosomal proteins, on average, declined more strongly than non-ribosomal cytoplasmic proteins (Fig. 1e, Fig. S1a-b). Consistently, proteins involved in translation, including but not restricted to ribosomes, declined more strongly than the average proteome (Fig. 1f). For LFQ-based measurements, no significant difference between the decline of mitochondrial and cytoplasmic proteins was observed (Fig. 1e). This difference between iBAQ and LFQ can occur when, on average, the more mass-abundant mitochondrial proteins have a faster relative decline. Indeed, abundant mitochondrial ribosomal proteins were among the most rapidly declining mitochondrial proteins (Fig. S1a). Yolk proteins also declined rapidly, consistent with their role in nutrient storage [30]. However, since only three yolk proteins were detected, contributing a mere 0.1% to the total detected proteome mass, the depletion of yolk was not statistically significant (Fig. 1e).

We next validated the mass-spectrometry-based measurements by luminescence-based detection using HiBiT [31] (Fig. 1b) and by live imaging. For HiBiT, we endogenously tagged the ribosomal protein RPL-17 and the yolk protein VIT-2 at their C-termini. Confirming measurements by mass-spectrometry, RPL-17 and VIT-2 declined rapidly (-7.0%/day and -10.9%/day) normalized to total protein (Fig. 1g), showing their preferential degradation compared to other proteins. The quantitative difference in decline rates observed with HiBiT and mass spectrometry may be due to technical differences, or due to biological differences among individual ribosomal proteins that are masked by the measurement noise of mass-spectrometry.

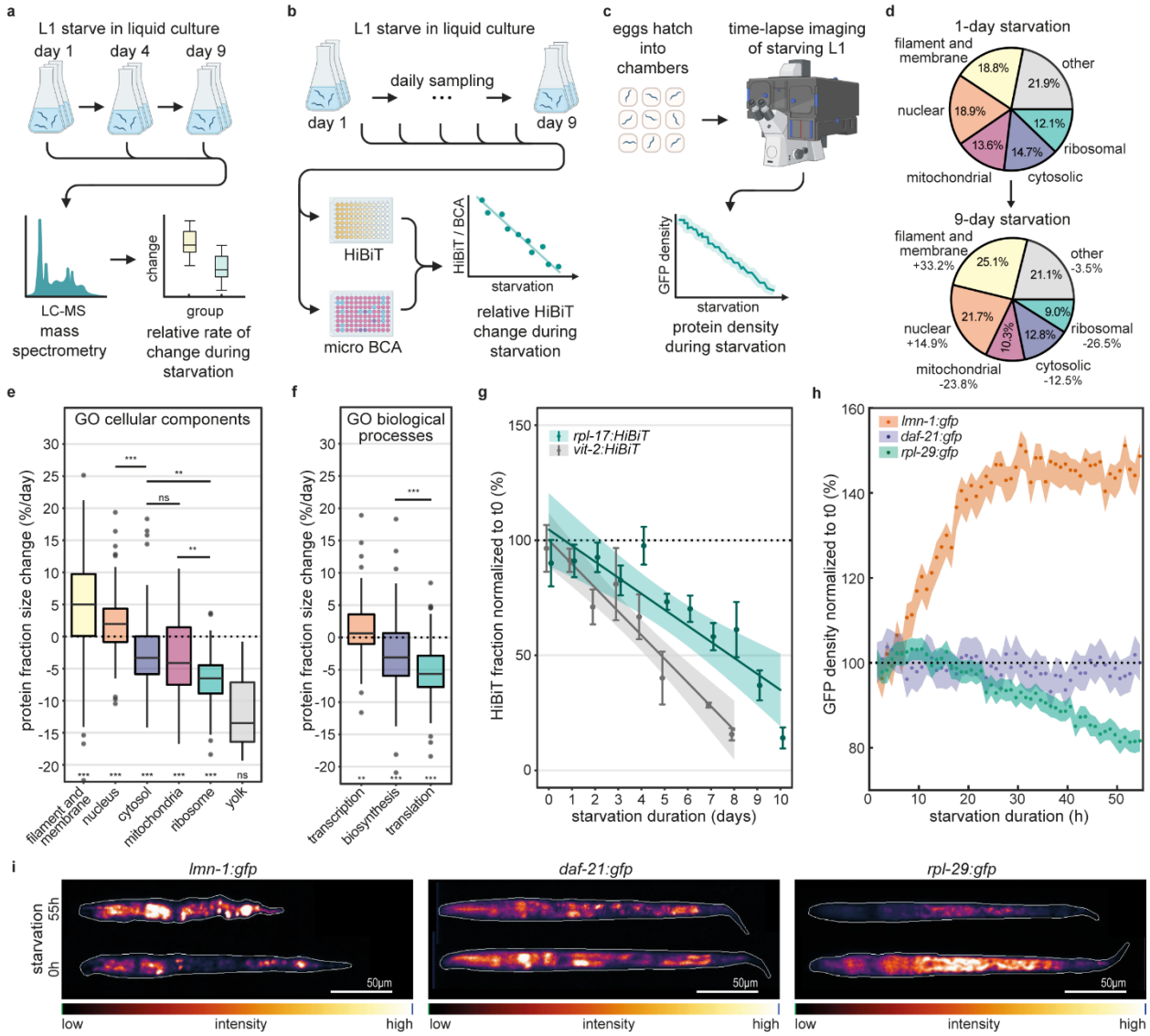

Figure 1. Rapid ribosomal protein decline during starvation. a-c. Experimental design of measurements of protein dynamics during starvation of L1 larvae by mass spectrometry (a) HiBiT (b) and live imaging (c). **d.** Mass fraction of indicated proteome subgroups on day 1 and day 9 of starvation (groups are based on GO cellular component annotation and quantified using iBAQ). Numbers inside sectors indicate mass fraction. Numbers outside sectors indicate the relative change in fraction size between days 1 and 9. **e,f**. Box plots of rates of change measured for individual proteins in indicated groups (quantified using LFQ). Stars above boxes: significance of comparison between groups (robust one-way ANOVA, adjusted post-hoc comparisons). Stars below boxes: difference to zero (adjusted Wilcox signed rank test) ***p<0.001 **p<0.01. **g**. Protein quantification by HiBit normalized to total protein at t = 0. error bars: s.e.m. from 3 biological repeats. line: linear regression (*rpl-17:HiBiT* r^2=0.94, *vit-2:HiBiT* r^2=0.79). shaded area: 95% CI of linear fit. **h.** Mean volumetric protein density of GFP-fluorescence over starvation time. shaded area: 95% CI. n = 146, 323 and 137 animals from 3 to 4 biological repeats for *lmn-1:gfp*, *daf-21:gfp* and *rpl-29:gfp*. **i.** Images of indicated strains after 0h and 55h starvation in agarose chambers. White: animal outline. Color scale: GFP intensity with equal contrast adjustment for the same genotypes. Animals were computationally straightened for display.

For live imaging, we created a strain with an endogenous GFP insertion in the ribosomal protein RPL-29, and used strains with integrated transgenes expressing the non-ribosomal cytoplasmic protein DAF-21:GFP[32] and the nuclear lamin LMN-1:GFP[33]. For each strain, we placed at least 100 eggs individually in

127 arrayed agarose-based chambers [34] that did not contain food. Upon hatching from the eggs, the starving
128 L1 larvae were imaged hourly by fluorescence microscopy for 55 hours, at an exposure that did not cause
129 significant photobleaching (Fig. S1c). We then determined the animal volume and fluorescent protein
130 concentration (fluorescence/volume) by computational segmentation and straightening [35]. In agreement
131 with proteomics data, the concentration of ribosomal RPL-29:GFP declined during starvation, nuclear LMN-
132 1:GFP increased in fluorescence, and cytosolic DAF-21:GFP fluorescence concentration remained
133 approximately constant (Fig. 1h,i & Fig. S1d-e). Taken together, the rate of decline varies among different
134 cytoplasmic proteins during starvation with ribosomal and translation-associated proteins being among
135 the most rapidly declining cytoplasmic proteins.

136 ***Preferential ribosomal protein decline is autophagy-dependent***

137 To test if the decline in ribosomal proteins required autophagy, we measured RPL-29:GFP in starving L1
138 larvae carrying mutations in the autophagy factors *atg-18*/WIPI or *unc-51*/ULK1 [29,36]. In both autophagy
139 deficient mutants, the decline of RPL-29:GFP was significantly slower than in wild type, albeit not
140 completely abolished (Fig. 2a). The residual decline was proportional to the overall decline in animal
141 volume, such that ribosome density was constant during starvation of these mutants (Fig. S2a-c). The
142 residual decline may be due to ribosomal protein degradation unrelated to autophagy, or due to residual
143 autophagic activity in the mutants. Importantly, although *atg-18* and *unc-51* are known to impair starvation
144 resistance [29,36], both mutants remained viable throughout the measurement period of 55 hours, as
145 determined by their motility and a lack of death-associated swelling [37] (Fig. S2a-b,d).

146 To determine the subcellular fate of ribosomal proteins, we created strains in which RPL-34 and RPL-22
147 were endogenously tagged with mCherry. Unlike GFP, mCherry remains fluorescent under the acidic
148 lysosomal conditions [38–40]. Upon starvation, RPL-34:mCherry (Fig. 2b) and RPL-22:mCherry (Fig. S2e)
149 became spatially heterogeneous (Fig. 2b,c & Fig. S2e,f), forming fluorescent foci. These foci were weaker
150 or absent in *atg-18* and *unc-51* mutants and no foci occurred for RPL-29:GFP in wild type animals (Fig.
151 2b,c), suggesting that mCherry foci represent accumulation in the acidic lysosomal compartment [40].
152 Consistently, 80% of RPL-34:mCherry foci were surrounded by, or co-localized with LMP-1:GFP, the *C.*
153 *elegans* homolog of the lysosome associated membrane protein (LAMP) [41] (Fig. 2d). We conclude that the
154 decline of ribosomal protein during starvation is largely autophagy dependent, and that ribosomal proteins
155 decline more rapidly than the average cytoplasmic proteome, consistent with the occurrence of an
156 autophagy pathway selective for ribosomes in *C. elegans*.

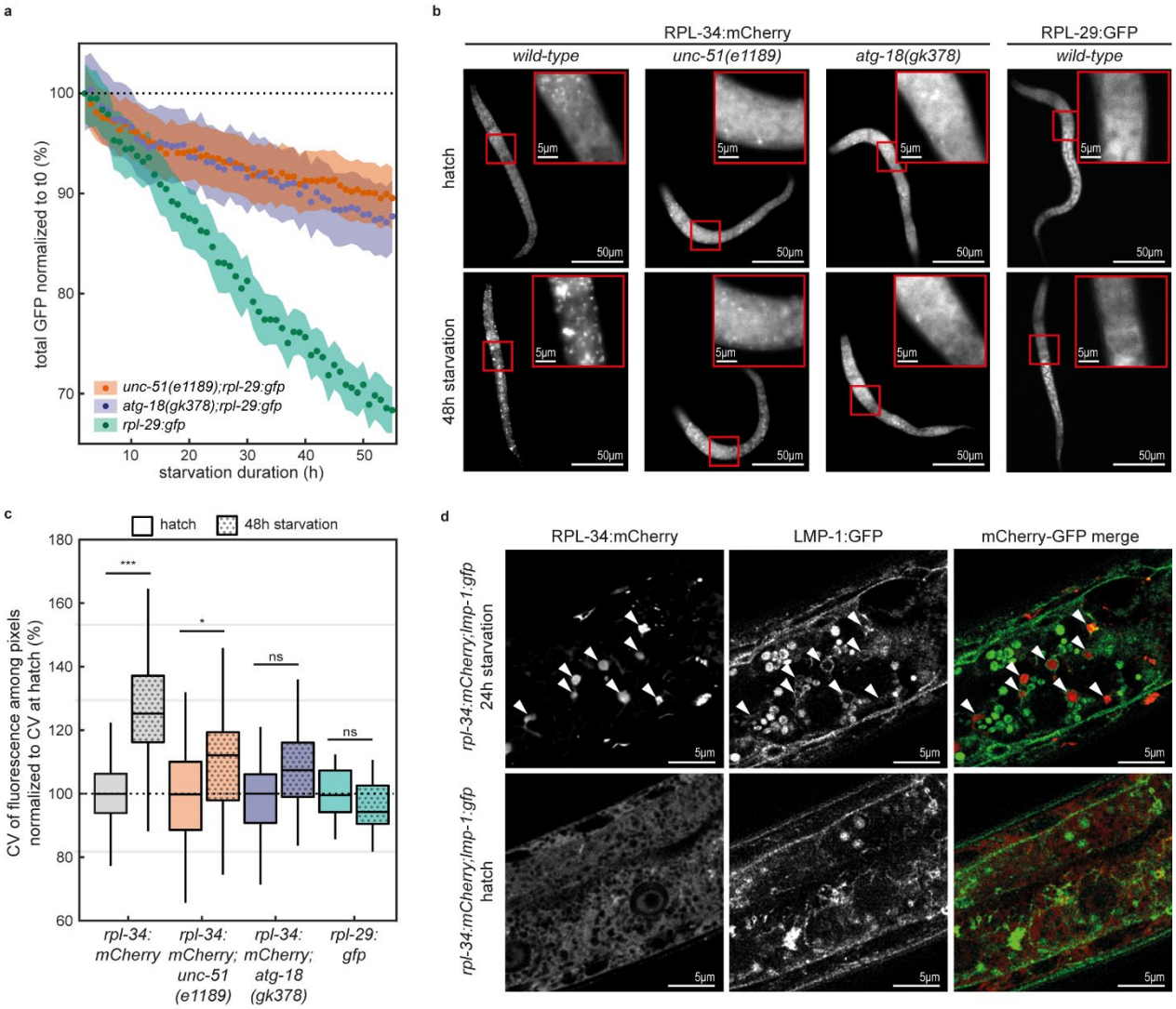

Figure 2. Ribosomal protein decline is autophagy-dependent. a. Total RPL-29:GFP fluorescence in wild type and in autophagy deficient animals during starvation. Mean and 95% CI of the mean for n = 283, 299, 101 animals from 3 biological repeats for *unc-51(e1189)* and *atg-18(gk378)* and 2 biological repeats for wild type. **b.** RPL-34:mCherry and RPL-29:GFP in wild type and autophagy deficient individuals at hatch and after 48h starvation. Contrast is equal for the same genotype. Focus formation is autophagy and starvation dependent, and only occurs for acid-insensitive mCherry, but not for GFP. **c.** Box plot of relative change in coefficient of variation (CV) among pixel intensities for strains and conditions shown in (b) (113, 49, 71, and 25 individuals per strain). Significance between group means (adjusted paired sample t-test): ***p<0.001, *p<0.05 (Table S1). **d.** Co-localization of RPL-34:mCherry and lysosomal membrane associated protein LMP-1:GFP at hatching and after 24h of starvation. Arrowheads: ribosomal foci, surrounded by LMP-1:GFP.

Ribosomal protein amount after starvation predicts recovery growth rate

To explore the impact of ribosomal decline on starvation survival and growth during recovery, we starved L1 larvae expressing RPL-29:GFP for 1, 3, and 6 days before feeding them in agarose chambers. By live imaging, we measured their organismal growth and ribosome expression at a time resolution of 15 minutes throughout development (Fig. 3a). In this assay, the larval molts of *C. elegans* (M1 to M4) can be detected by a halt in volume growth prior to ecdysis [34,42] (Fig. 3b), allowing precise determination of the larval stage durations. Consistent with previous reports [43], starvation delayed the completion of the L1 stage by

approximately two hours per day of starvation (Fig. 3c). This lag time was inversely correlated (r^2=0.87) with the total RPL-29:GFP fluorescence measured at the first time point of feeding (Fig. 3d,e). The correlation occurred across different durations of starvation, and across individuals exposed to the same duration of starvation (Fig. 3d). Thus, regardless of the starvation conditions experienced, the remaining RPL-29:GFP after starvation predicted the time a given individual needed to complete the first larval stage with high accuracy (Fig. 3d). RPL-29:GFP fluorescence also correlated with body volume, but the observed correlation between growth and RPL-29:GFP level was not due to volume differences alone. The correlation between animal volume and larval stage duration was weaker than that between total RPL-29:GFP and larval stage duration (r^2 = 0.67 vs. r^2 = 0.85, Fig. S3a). Moreover, we also detected a significant correlation (r^2=0.64) between the larval stage duration and the RPL-29:GFP density (GFP/volume) (Fig. S3b). During the first larval stage, starved animals recovered ribosomes to near normal levels (Fig. S3c). Consistently, starvation duration had a small or no effect on larval stage durations, growth rates, ribosome expression, and body volumes from the second larval stage onwards (Fig. 3b, Fig. S3c-d).

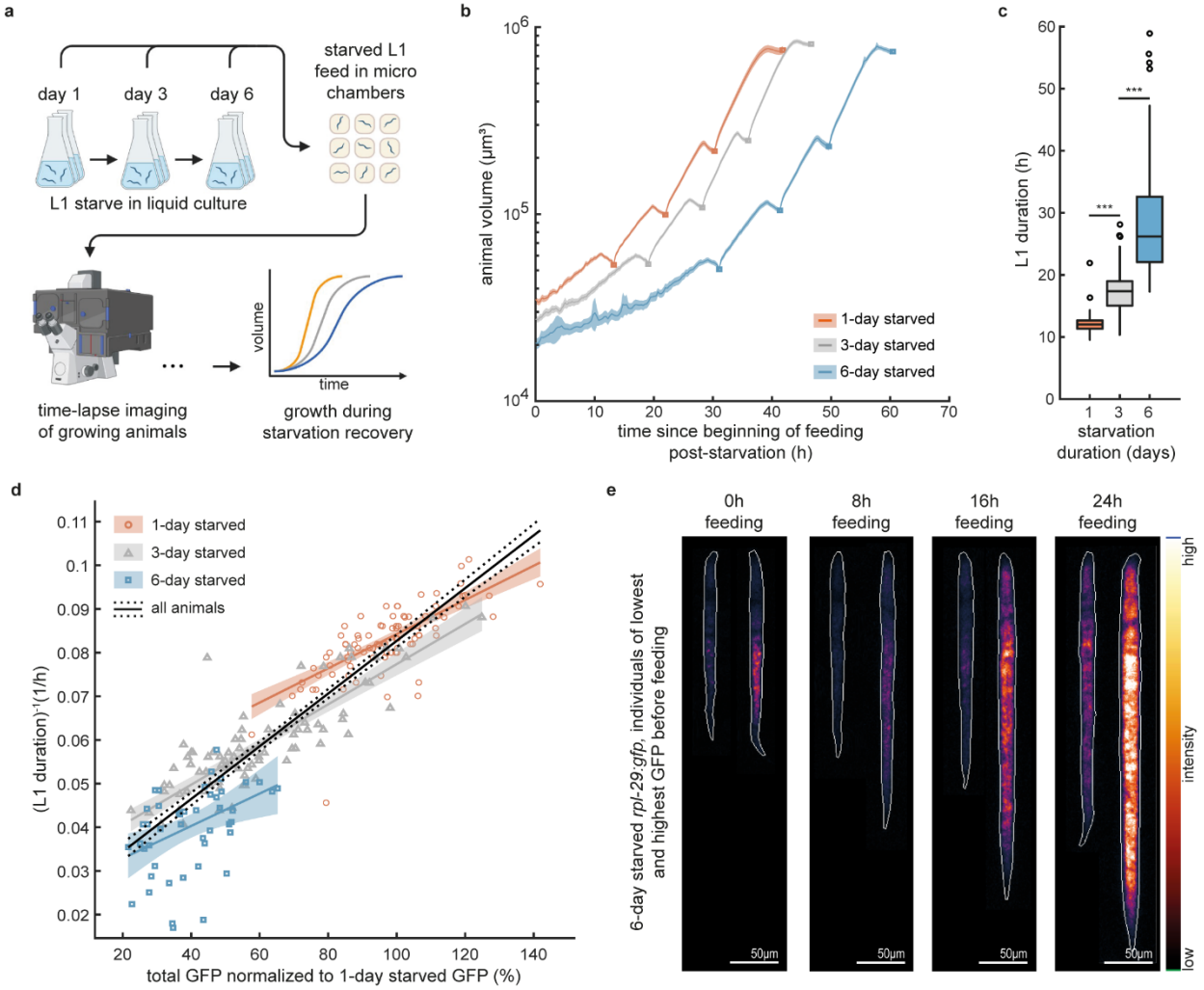

Figure 3. Ribosome level predicts recovery speed. a. Experimental design of starvation recovery measurements. **b.** Mean animal volume during post starvation feeding after 1, 3 and 6-day starvation for n = 67, 66 and 43 indivduals. Squares: molts between larval stages. Shaded area: 95% CI of the mean. Means were computed by aligning individual trajectories to the molts prioir to averaging, followed by re-scaling to the mean larval stage duration. **c**. Box plots of L1 duration after 1, 3 and 6-day starvations for 89, 89 and 71 individuals, respectively. Significance between group

means (two sample t-test): ***p<0.001 (Table S1). **d.** RPL-29:GFP fluorescence vs. the inverse of the L1 larval stage duration after recovery from 1, 3 and 6-day starvation for 85, 83 and 44 individuals. Lines: linear correlation with 95% CI. Black: all starvation durations pooled (r^2=0.85). blue, gray, red: separated by starvation duration (r^2=0.62, r^2=0.76 and r^2=0.19 for 1, 3, and 6-days). **e.** Images of the individuals expressing the highest and the lowest RPL-29:GFP after 6-day starvation at indicated times of feeding. Contrast is matched for animals at the same time of feeding. White: body outline. Color scale: GFP intensity. Animals were computationally straightened for display.

We conclude that the level of ribosomes remaining after starvation is a good predictor for the rate at which L1 larvae resume development. Our data suggests that the need to re-synthesize degraded ribosomes, and possibly other proteins required for growth, slows down recovery from starvation.

Hyperactivation of the mTORC1 activator RAGA-1 reduces ribosomal decline

To slow-down ribosomal protein decline experimentally during starvation, we genetically engineered the mTORC1 activator Ras-related GTP-binding protein A (RAGA-1), the single *C. elegans* ortholog of mammalian RagA/B [44]. RAGA-1 normally switches from a GTP to a GDP bound state upon amino acid starvation, which represses mTORC1 activity. We introduced a mutation that stabilizes the GTP bound form, hereafter called RAGA-1^{GTP}, that constitutively activates mTORC1 regardless of amino acid availability[45], and ultimately upregulates biosynthetic pathways and inhibits autophagy [46] (Fig. 4a).

To test if RAGA-1^{GTP} animals retained ribosomes during starvation, we conducted quantitative label-free proteomics in wild type and mutant animals side-by-side. We sampled on days 1, 4, and 7, during which viability of RAGA-1^{GTP} animals was not compromised compared to wild type (Fig. 4h, Fig. S5f). The RAGA-1^{GTP} mutation significantly dampened the decline in the mass fraction of ribosomal proteins estimated by iBAQ (Fig. 4b-c, -32.8%, s.e.m. = 1.4% vs. -17.1%, s.e.m. = 1.8%, $\Delta_{(WT - RAGA\text{-}1\text{-}GTP)}$ = -15.7%). RAGA-1^{GTP} had a much smaller effect on the decline of cytoplasmic and mitochondrial proteins (Δ = -6.3% for both, Fig. 4b-d), suggesting that this mutation reduces the selectivity of ribophagy.

We note that the proteome mass fraction sizes differed between our initial measurements of wild type alone (Fig. 1d) and when measured for comparison with RAGA-1^{GTP} (Fig. 4b-c). These differences may be due to experimental batch effects or due to the higher number of proteins detected in the latter experiment (2789 and 2052 proteins for iBAQ and LFQ). Importantly, both experiments consistently show that ribosomes decline more rapidly than the average cytoplasm in wild type animals.

Consistent with changes in proteome fractions, the median rate of decline of individual ribosomal proteins (based on LFQ) was faster in wild type than in RAGA-1^{GTP} animals (-9.7%/day vs. -6.0%/day, Δ = -3.7%/day, Fig. 4d). This difference between RAGA-1^{GTP} and wild type was similarly pronounced for proteins associated with translation in general (Δ = -3.2%/day, Fig. S4c), but less pronounced for mitochondrial proteins (Δ = -1.3%/day), non-ribosomal cytosolic proteins (Δ = -1.1%/day), yolk proteins (Δ < 0.1%/day), and various nuclear components (Fig. 4d & Fig. S4a). Thus, *raga-1* influenced the turnover of ribosomal proteins more strongly than that of other proteins (Fig. 4b-d & Fig. S4a-b).

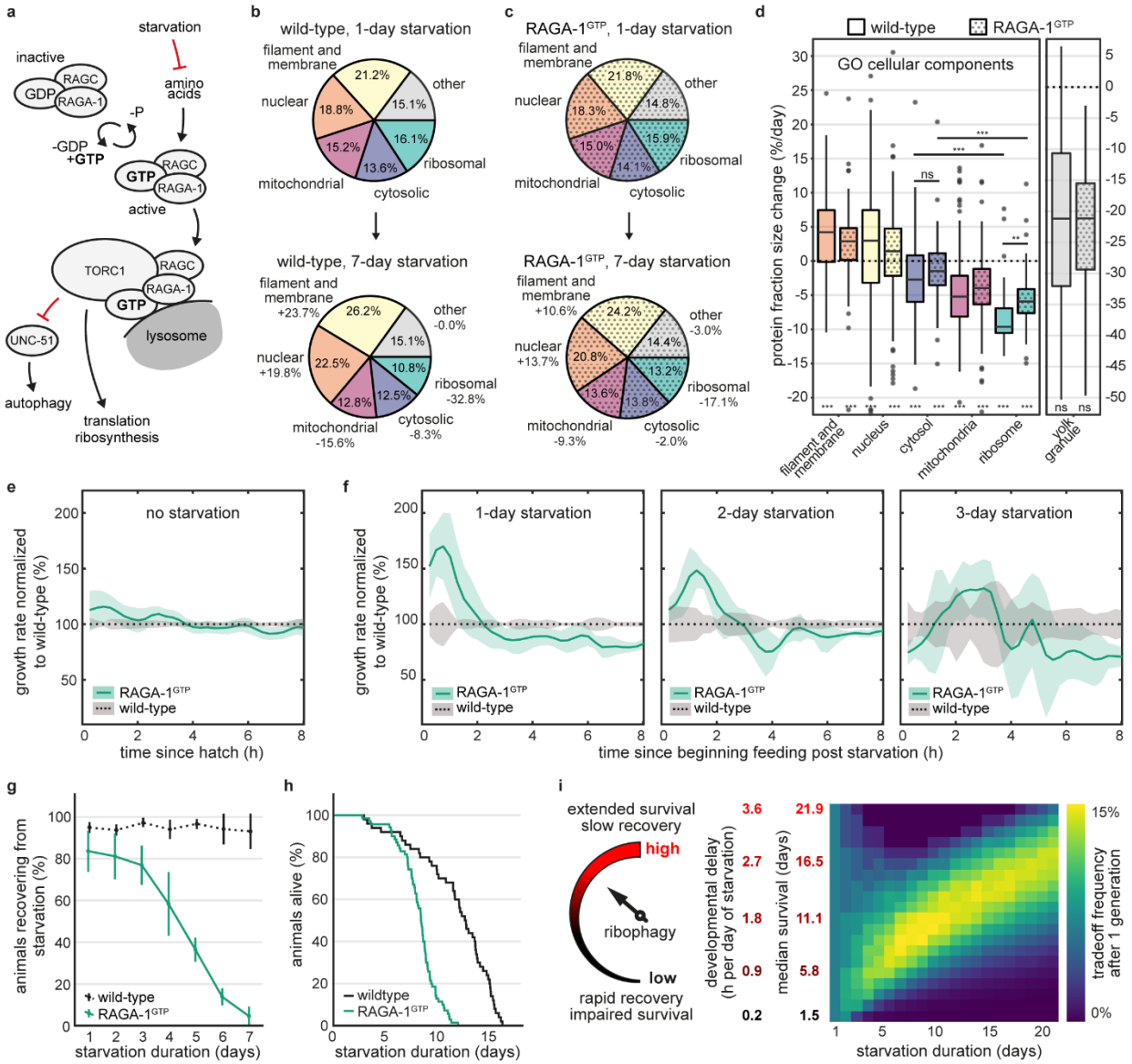

Figure 4. Reducing ribophagy shifts a tradeoff between starvation survival and recovery: a. Schmatic of RAGA-1 in mTORC1 signalling. **b,c**. Quantification of proteome mass fractions on day 1 and 7 of starvation as described in Fig. 1, but for wild type and RAGA-1^{GTP} animals. Percentages inside sectors indicate group fraction size. Percentages outside sectors indicate proportional change in fraction size from the 1st day to the 7th day of starvation. **d.** Box plots of rates of decline for individual proteins grouped by GO cellular component-terms for wild-type (solid fill) and RAGA-1^{GTP} (dotted fill). Stars above boxes: differences between group means (robust two-way ANOVA, adjusted post-hoc comparison). Stars below boxes: difference to zero (adjusted Wilcox signed rank test). (***p<0.001, **p<0.01). **e,f**. Ratio of relative growth rate ((dV/dt)/V) between RAGA-1^{GTP} and wild type animals during *ad libitum* feeding after hatching (e) and after indicated duration of starvation (f) for the first 8 hours of feeding. Solid line: mean of 177 to 386 individuals across 2 to 5 biological repeats per strain and condition. Shaded area: 95% CI of the mean. **g**. Fraction of individuals that successfully recovered growth after indicated starvation duration. A total of 3467 wild type and 2621 RAGA-1^{GTP} individuals were sampled across 3 biological repeats. **h.** Starvation survival in agarose chambers. 48 wildtype and 70 RAGA-1^{GTP} animals. **i**. Proposed model: trade-off between starvation survival and starvation recovery is tuned by the selectivity of autophagy towards ribosomes and possibly other proteins required for translation and growth. Heatmap shows simulated relative population growth for competing strains with different growth and

survival balances (rows) under different durations of starvation (columns). The optimal compromise that maximizes selective fitness (yellow) depends on the duration of starvation.

We confirmed these data by live imaging. Immediately after hatching, RPL-29:GFP expression was 10% higher in RAGA-1^{GTP} animals than in wild-type animals (Fig. S4d-e), consistent with mTORC1 hyperactivation. Throughout 55 hours of starvation, RPL-29:GFP total fluorescence, fluorescence relative to the starting levels, and volumetric density remained higher in RAGA-1^{GTP} (Fig. S4d-g). RAGA-1^{GTP} did not significantly affect the body volume during starvation (Fig. S4h-i), consistent with a quantitative reduction of ribophagy by RAGA-1^{GTP}, rather than a total halt of bulk autophagy (Fig. 4b-d). Measurement of protein production rates by photo-bleaching [47] showed that RPL-29:GFP production during starvation was negligible in mutant and wild type animals (Fig. S5a-d). The difference in the rate of decline between mutant and wild type are therefore not due to differences in ribosomal protein synthesis, but due to different rates of degradation. Differences in fluorescence between RAGA-1^{GTP} and wild type were also not explained by a GFP tag associated with the RAGA-1^{GTP} mutation, since the expression of this tag was near negligible compared to that of RPL-29:GFP (Fig. S5e). Together, we conclude that hyperactivation of mTORC1 activity by RAGA-1^{GTP} slows down the starvation-induced decline of ribosomal proteins and possibly of other translation associated proteins.

RAGA-1^{GTP} impairs starvation resistance and speeds up growth during recovery

Consistent with previous findings in mice [48], RAGA-1^{GTP} mutants had reduced starvation resistance with more than 50% of the animals failing to recover growth after 5 days of starvation (Fig. 4g), and a sharp drop of viability (based on motility) after 9 days (Fig. 4h). To test if impaired survival during long starvation was paralleled by a faster recovery of RAGA-1^{GTP} animals after short starvation, we measured the growth rate of wild-type and RAGA-1^{GTP} animals in agarose chambers without starvation and after 1, 2, and 3 days of starvation. We observed no significant difference in the growth rate of RAGA-1^{GTP} and wild-type animals that were not exposed to starvation (Fig. 4e). However, after 1 and 2 days of starvation, RAGA-1^{GTP} mutants grew significantly faster than wild-type during the first two hours of recovery (Fig. 4f, Fig. S6a-b,i-j). This growth advantage of RAGA-1^{GTP} was transient and disappeared later in development when wild type animals had reconstituted their ribosomes (Fig. S6c-f). Thus, although the RAGA-1^{GTP} did not accelerate growth *per se*, the mutation accelerated recovery from starvation, possibly by retaining higher levels of ribosomes. No significant growth benefit of RAGA-1^{GTP} animals was observed after 3 days of starvation (Fig. 4f & Fig. S6b,i,j), possibly due to an increased frailty of this mutant after longer starvation (Fig. 4g,h) or a smaller difference in ribosome levels between wild type and mutant after 3 days of starvation (Fig. S6e,f).

Together, these data show that hyperactivation of RAGA-1 accelerates growth during recovery after short periods of starvation but impairs growth and survival after longer starvation periods. The balance between the retention of ribosomal proteins, and possibly other translation factors, and their degradation to fuel metabolism provides a parsimonious explanation for the widely observed tradeoff between growth and survival [5,6,8,49–51] (Fig. 4i).

Best compromise between recovery speed and survival depends on starvation duration

To explore under which conditions a rapid recovery may be favorable compared to a high starvation survival, we simulated population growth using realistic life-history parameters for *C. elegans* in a mathematical model. In the model, starvation caused a developmental delay τ that increased linearly with time ($\tau = \delta * t$), as experimentally observed [43]. We modelled starvation survival by Hill function with half-point σ matching measured data (Fig. 4h). To model the tradeoff, δ and σ were proportionally coupled ($\delta \propto \sigma$). Strains with different tradeoff strategies were competed against each other until the total population

287 had expanded 20-fold (representing food exhaustion). These simulations showed that a longer median
288 survival σ at the cost of a longer delay τ were beneficial for long durations of starvation (Fig. 4i) whereas a
289 short delay and short survival were beneficial for short durations of starvation. The optimal compromise
290 between growth and survival thus depends on the duration of starvation periods, suggesting that the
291 ribophagy rate is an adaptive trait whose optimal value depends on the specific starvation regime.

292 **Discussion**

293 In a dynamic nutritional environment, the ability to survive extended starvation and to rapidly resume
294 growth when encountering food is crucial for organismal fitness. In the face of tradeoffs, these tasks must
295 be optimally balanced, in accordance with the frequency and duration of starvation periods. Evidently, if
296 episodes of starvation are long, it is crucial to be able to survive long periods without food. However, if the
297 expected duration of starvation is short, a strategy that accelerates growth resumption at the expense of
298 survival may be advantageous (Fig. 4i). Here, we employed quantitative assays to reveal a mechanism by
299 which *C. elegans* can adjust the balance between these key aspects of organismal physiology.

300 We showed that *C. elegans* selectively catabolize ribosomal proteins during starvation through autophagy
301 (Figs. 1 & 2), a process called ribophagy [18]. This strategy enhances survival by providing energy without
302 degrading essential cellular components but comes at the cost of delayed growth resumption upon
303 refeeding (Figs. 3 & 4). Notably, the synthesis of ribosomal proteins itself depends on functional ribosomes.
304 The loss of ribosomes therefore not only impairs the onset of growth, but also the re-synthesis of
305 ribosomes themselves. This combined effect may explain the observed developmental delay of up to
306 several days following recovery from starvation [43,52].

307 Unlike other pathways of selective autophagy [53], the mechanisms governing ribophagy are only beginning
308 to be characterized [24]. While amino acid starvation is known to induce ribophagy in yeast [18], the specific
309 receptor mediating this process has not been identified. In mammalian cells, the protein NUFIP1 has been
310 proposed as a ribophagy receptor[21], but conflicting evidence has cast doubt on its role [20]. Similarly, it
311 remained contentious to what extent selective ribophagy indeed contributes to the decline in ribosomes
312 relative to unspecific bulk autophagy [19,22]. Importantly, our study not only demonstrates that ribosomes
313 are degraded by autophagy during *C. elegans* starvation (Fig. 2), but also that the rate of ribophagy is faster
314 than the bulk degradation of other cytoplasmic proteins (Fig. 1). Moreover, genetically manipulating the
315 ribophagy rate directly impacted both starvation survival and the speed of growth recovery (Fig. 4). These
316 findings firmly establish the biological relevance of regulated ribosomal turnover in a physiological context,
317 providing a foundation for future investigations of its molecular control.

318 Quantitative studies of growth-survival tradeoffs have primarily focused on bacteria [4,5], where the growth
319 rate follows a linear relation with the ribosomal protein content [11]. This simple relation has enabled
320 accurate predictions of cellular growth dynamics when switching between conditions [10,54,55], that did not
321 rely on modelling the thousands of molecular reactions controlling cellular growth. Our data in *C. elegans*
322 reveal a similarly linear relationship between ribosome levels and the speed of growth recovery from
323 starvation (Fig. 3). This finding suggests that the core principles governing proteome partitioning and
324 growth control are portable from the microbial to the multicellular scale, at least for *C. elegans*, enabling
325 coarse-grained models of organismal biology.

326 It is important to note that the partitioning of the proteome between different functions is not restricted
327 to ribosomes. Indeed, we find that also other translation-related proteins are rapidly catabolized during
328 starvation (Fig. 1) and may also be limiting for growth recovery. Similarly, the genetic modulation of mTOR

329 signalling through *raga-1* did not only impact ribophagy, but also the turnover of other proteins required
330 for growth and translation (Fig. 4). Whereas our current live imaging measurements have focused on
331 ribosomal proteins, ribosomes evidently are not the only proteins required for growth but serve here as a
332 representative example of growth-enhancing proteins more generally. Whether the selectivity of
333 autophagy towards ribosomes and other translation factors is controlled by the same or by independent
334 mechanisms presents an important mechanistic question for future studies.

335 In addition to the tradeoff between starvation survival and growth resumption examined in this study, the
336 proteome resource allocation to ribosomes may also be important for other organismal tradeoffs. For
337 instance, the striking correlation between the translation rate and lifespan [56] indicates that a similar
338 mechanism may underlie the well-known tradeoff between growth and longevity. In this context, high
339 production of ribosomes may accelerate growth but sequester resources from expression of survival-
340 enhancing proteins that counteract aging. The quantitative methodology and framework established here
341 now empower us to systematically address this hypothesis and uncover the full scope of proteome
342 partitioning in shaping diverse organismal tradeoffs.

343 An important question raised by our work is how environmental conditions shape the evolution of selective
344 ribophagy. Our theoretical analysis predicts that the best compromise between starvation survival and
345 rapid growth resumption depends on the average duration of starvation periods. One would thus expect a
346 rapid ribophagy rate in strains adapted to long starvation periods, while adaptation to shorter periods of
347 starvation should favor the preservation of ribosomes, which would facilitate rapid growth resumption.
348 Our molecular characterization of ribophagy in an organismal context opens exciting opportunities to test
349 these predictions and understand how molecular processes shape the evolution of growth and survival
350 along organismal tradeoffs.

351 **Materials and Methods**

352 ***C. elegans strains and maintenance***

353 Animals were grown and maintained at 25°C using OP50-1 *E. coli* on nematode growth medium (NGM)
354 according to standard procedures. The following strains were used in this study:

355 WBT100: *rpl-17(xe232)[rpl-17:HiBit]; xeSi296[peft-3::luc-gfp::unc-54 3'UTR, unc-119(+)] II* (this study),
356 used in Fig. 1a-b,d-g, Fig. S1a-b, Fig. S7a,c-f

357 WBT203: *vit-2(syb3768)[vit-2::GSSG::3xflag::GSSG::HiBiT] X* (this study), used in Fig. 1g

358 GW8: *ygIs[lmn-1::GFP::lmn-1 unc-119(+)] X; unc-119(ed3) III* ([33]), used in Fig. 1c,h-i, Fig. S1d-e

359 RBW2661: *hutSi2661 [hsp-90p::eGFPT::unc-54 3'UTR + Cbr-unc-119 (+)] II* ([32]), used in Fig. 1c,h-i, Fig. S1d-
360 e

361 PHX1945: *rpl-29(syb1945) [rpl-29:GFP]* (this study), used in Fig. 1c,h-i, Fig. 2a-c, Fig. 3, Fig. 4e-g, Fig. S1c-
362 e, Fig. S2a-d,f, Fig. S3, Fig. S4d-i, Fig. 5Sf, Fig. S6a-b,e-f, Fig. S6

363 N2: Bristol N2 wild isolate, used in Fig. 1c,g-i, Fig. S1d-e, Fig. S5a-e

364 WBT257: *rpl-29(syb1945) [rpl-29:GFP] IV; unc-51(e1189) V* (this study, allele e1189 from CGC registered
365 strain CB1189 by J. A. Hodgin lab, Oxford University), used in Fig. 2a, Fig. S2a-c,f

366 WBT277: *rpl-29(syb1945) [rpl-29:GFP] IV; atg-18(gk378) V* (this study, allele gk378 from [57]), used in Fig.
367 2a, Fig. S2a-c,f

368 PHX1880: *rpl-34(syb1880) [rpl-34:RPL-34:mCherry] IV* (this study), used in Fig. 2b-c, Fig. S2f

369 PHX1903: *rpl-22(syb1903) [rpl-22:RPL-22:mCherry] II* (this study), used in Fig. S2e

370 WBT230: *rpl-34(syb1880) [rpl-34:RPL-34:mCherry] IV; unc-51(e1189) V* (this study, allele e1189 from CGC
371 registered strain CB1189 by J. A. Hodgin lab, Oxford University), used in Fig. 2b-c

372 WBT234: *rpl-34(syb1880) [rpl-34:RPL-34:mCherry] IV; atg-18(gk378) V* (this study, allele gk378 from [57]),
373 used in Fig. 2b-c

374 WBT343: *unc-119(ed3)III; pwls50[lmp-1p::lmp-1::GFP+Cb-unc-119(+)]; rpl-34(syb1880) [rpl-34:RPL-*
375 *34:mCherry] IV* (this study, allele pwls50 from CGC registered strain RT258 by B. D. Grant lab, Rutgers
376 University), used in Fig. 2d

377 WBT64: *xeSi296 [Peft-3::luc::gfp::unc-54 3'UTR, unc-119(+)] raga-1(xe190) II* (this study, allele xeSi296
378 from [58], allele xe190 from [45]), used in Fig. 4b-d, Fig. 4Sa-c, Fig. S7b,g-i

379 HW1939: *xeSi296 [peft-3::luc::gfp::unc-54 3'UTR, unc-119(+)] II* ([58]), used in Fig. 4b-d, Fig. 4Sa-c, Fig.
380 S7b,g-i

381 WBT330: *raga-1(wbm40) [raga-1::AID::EmGFP] II; xeSi376ubs38[Peft-3::TIR1(*ubs38 *[F79G])::mRuby::unc-*
382 *54 3'UTR, cb-unc-119(+)] III; rpl-29(syb1945) [rpl-29:GFP] IV* (this study, allele xeSi376ubs38 from [59]), used
383 in Fig. 4h, Fig. S5f

384 WBT289: *raga-1(wbm40abt3) [raga-1(GF)::AID::EmGFP] II;* xeSi376ubs38*[Peft-3::TIR1(*ubs38
385 *[F79G])::mRuby::unc-54 3'UTR, cb-unc-119(+)] III; rpl-29(syb1945) [rpl-29:GFP] IV* (this study, allele
386 xeSi376ubs38 from [59]), used in Fig. 4b-h, Fig. S4d-i, Fig. S5c-f, Fig. S6

387 WBT231: *raga-1(wbm40abt3) [raga-1(GF)::AID::EmGFP] II* (this study), used in Fig. S5e

388

389 ***Egg collection and starvation cultures***

390 Animals were grown on NGM plates at 25°C for at least 3 generations prior to starvation. For mass
391 spectrometry experiments, the peptone concentration in NGM was increased to 20mg/ml to reach
392 sufficient numbers of individuals. Mixed populations were synchronized by bleaching and the eggs were
393 allowed to develop into gravid adults on new plates. The adults were filtered with a cell strainer with 40µm
394 mesh size (Pluriselect) to remove younger animals and incubated in 35mM serotonin in S-basal in a rotating
395 cradle at 25°C for 1.5h. Eggs were harvested and separated from adults with a 40µm mesh, and the eggs
396 were filtered a 20µm mesh (Neolab) to remove hatched L1 larvae. The purified eggs were then either
397 loaded into agarose chambers for timelapse imaging or allowed to hatch overnight in S-basal (without
398 cholesterol and ethanol) in a rotating cradle at 25°C at a concentration of 10 eggs/µl. The following day,
399 the hatched L1 larvae were filtered with 20µm mesh to remove unhatched eggs. The L1 larvae were then
400 starved in S-basal (without cholesterol and ethanol) in a rotating cradle at 25°C at a density of 10 L1/µl for
401 the remainder of the starvation duration.

402 For mass spectrometry experiments, the synchronized gravid animals were bleach synchronized instead of
403 serotonin treated to obtain eggs. The eggs were allowed to hatch overnight in S-basal (without cholesterol
404 and ethanol) in an orbital shaker at 25°C at a concentration 10 eggs/µl. The hatched L1 larvae were filtered
405 with a 20µm mesh to remove unhatched eggs. The L1 larvae were starved in sterile S-basal cultures

406 (without cholesterol and ethanol) in orbital shaker at 25°C at 10 L1/µl for the remainder of the starvation
407 duration.

408 ***Unlabeled mass spectrometry***

409 Starving L1 larvae were collected (10^6 animals/sample) from triplicate cultures (S-basal without cholesterol
410 and ethanol at 25°C in orbital shaker at 10 animals/µl) and resuspended into 700µl PBS without additives.
411 The pellets were flash frozen by pipetting dropwise into liquid nitrogen. Frozen beads were powdered using
412 cryogenic SPEX SamplePrep 6775 Freezer/Mill and stored as frozen powder at -80°C.

413 Powdered pellets were dissolved in 1% sodium deoxycholate buffer containing 50 mM Tris-HCl pH 8.
414 Samples were treated with 1 mM DTT and alkylated using 5.5 mM iodoacetamide for 10 min at RT. Samples
415 were in-solution digested with trypsin (Promega). Tryptic peptides were purified by STAGE tips and LC-
416 MS/MS measurements were performed on a QExactive plus and an Orbitrap Exploris 480 mass
417 spectrometer coupled to EasyLC 1200 nanoflow-HPLCs (all Thermo Scientific) using data-dependent
418 acquisition. MaxQuant software (version 1.6.2.10 & 2.0.1.0) [60] was used for analyzing the MS raw files
419 performing peak detection, peptide quantification and identification using a Uniprot *C. elegans* database,
420 November 2017. Carbamidomethylcysteine was set as fixed modification and oxidation of methionine was
421 set as variable modification. The MS/MS tolerance was set to 20 ppm and four missed cleavages were
422 allowed for Trypsin/P as enzyme specificity. Based on a forward-reverse database, protein and peptide
423 FDRs were set to 0.01, minimum peptide length was set to seven, and at least one unique peptide had to
424 be identified. MaxQuant results were analysed using Perseus software (version 1.6.2.3)[61]. iBAQ and LFQ
425 values were used for expression proteomics analyses. iBAQ values of the respective samples were median
426 normalized. Only proteins with valid values in all three biological replicates in respective groups were
427 considered for further analysis.

428 iBAQ and LFQ data were analyzed using R-studio (v4.3.2). Mass fractions were determined by multiplying
429 iBAQ quantification of each detected protein by its molecular weight. Resulting mass values were grouped
430 and summed based on GO terms and divided by the total iBAQ mass. Molecular weights and GO terms
431 were acquired from UniProtKB by list search of protein IDs reported by MaxQuant. The rate of change for
432 individual proteins was computed by the slope of a linear best fit through logarithmic LFQ fraction
433 measurements. Slopes of individual proteins were grouped based on whether the GO terms associated
434 with the protein matched category presented in Fig. 1d-f and 4d (e.g. "ribosome"). For figures shown in
435 main text, each protein was allowed to appear in only one group (see Table S2 for list of proteins in each
436 group). Equivalent analysis allowing for group overlap is shown in supplemental material (Fig. S7c-e).

437 ***HiBiT measurements***

438 Starving L1 larvae were collected (3000 animals/sample) from triplicate cultures into 100µl lysis buffer (PBS
439 pH8, 0.25% triton, protease inhibitors (Sigma P8340)), and freeze-thawed three times in liquid nitrogen
440 and 37°C water bath. Samples were lysed by sonication (Bioruptor) at 4°C and diluted with 600 µl PBS prior
441 to HiBiT assay.

442 After lysis all pipetting was conducted using motorized pipettes (Sartorius) and a pipetting robot (Opentron)
443 to minimize experimental variation. HiBiT intensity was measured daily in three biological replicates (3
444 measurements x 3 wells x 3 replicates / day) in 384-well format using a HiBiT quantification kit (Promega
445 Nano-Glo). 5µl HiBiT reaction mixture (1:100 LgBiT protein and 1:50 HiBiT lytic substrate in HiBiT lytic
446 buffer) was combined with 5µl sample. Plates were shaken at room temperature for 5min prior to
447 measuring luminescence on a luminometer (SpectromaxL).

448 Protein concentration in each sample was measured using micro-BCA kit (Pierce) in three biological
449 replicates (3 measurements x 3 wells x 3 replicates / day) in 96-well format. 140ul sample was combined
450 with 140ul BCA reagent (25:24:1 mix of reagents MA:MB:MC) at 4°C. The plates were shaken for 5min,
451 incubated stationary in 37°C incubator for 2h, and measured with Spectromax340 562nm in endpoint
452 mode.

453 Data analysis was done in R (v4.3.2). Background signals were subtracted (BCA reagent with lysis buffer for
454 micro-BCA, N2 worm lysate with reaction mixture for HiBiT) and HiBiT measurements were normalized
455 with total protein BCA measurements to acquire HiBiT fraction. The fractions were normalized again by the
456 average of the 3 biological replicates at t=0 and a linear model was fitted to the normalized values.

457 ***Live imaging in agarose-based chambers***

458 Arrayed agarose chambers were manufactured by stamping a microscopic chamber pattern into gel of 4.5%
459 agarose in S-basal using a PDMS template (Wunderlichips) based on Turek et al. [62], incorporating the
460 modifications by Stojanovski et al. [34]. Animals were retained isolated in separate chambers and imaged
461 every hour for starvation experiments, and every 15 minutes for post-starvation growth experiments.
462 Chamber dimensions were 270x270x20µm for L1 starvation experiments in Fig. 1, Fig. 1S, Fig. 2 and Fig.
463 2S. Chamber depth was decreased to 10µm for L1 starvation experiments in Fig. 4S and for all L1 starvation
464 recovery experiments in Fig. 4 to improve image focus, accuracy of segmentation, and volume estimates.
465 Chamber dimensions were increased to 600x600x20µm for post-starvation growth experiments in Fig. 3
466 and Fig. S3 to accommodate animal growth at L3 and L4 stages.

467 For starvation experiments, the chambers were manufactured without adding cholesterol and ethanol to
468 the agarose. 0.003% Triton was added to the eggs to reduce clumping and the eggs were pelleted. The egg
469 pellet was gently broken up before pipetting 5µl concentrated eggs onto freshly manufactured chambers.
470 2-fold or older eggs inside a droplet of S-basal without cholesterol or ethanol were then individually guided
471 to chambers using an eyelash pick.

472 For post-starvation growth experiments, chambers were filled with OP50-1 *E. coli* by scraping an *E. coli*
473 lawn off a standard NGM plate and spreading it onto the chambers with a piece of 3% agarose gel prior to
474 loading animals as described by Stojanovski et al. [34]. In Fig. 4, the agarose of the chambers contained 0.05%
475 DMSO. Starved L1 larvae were pipetted next to the array of chambers and then moved individually to
476 chambers using an eyelash pick. Chamber array was prevented from drying during loading by pipetting
477 20µl deionized water around the outer perimeter of the chamber array.

478 After loading animals into the chambers, the agarose chambers were inverted onto dishes with gas
479 permeable polymer bottom of high optical quality (Ibidi) and surrounded by 3% low melting temperature
480 agarose. The assembly was covered with thin layer of PDMS to prevent evaporation and the dish was closed
481 and sealed with parafilm and used for imaging.

482 A Nikon Ti2 wide-field epifluorescence microscope equipped with a SpectraX light source (Lumencor) and
483 a Prime BSI camera (Photometrics) was used for all live imaging experiments. A 10x 0.45NA objective was
484 used in Fig. 3b-e, Fig. S3a-d, Fig. S4e-g, and Fig. S6. A 20x 0.75NA objective was used in Fig. 1h-I, Fig. S1c-
485 e, Fig. 2a-c, Fig. S2a-f, and Fig. S5a-h. Effective pixel size in the sample plane was 0.65 and 0.325µm,
486 respectively. Software auto-focus of NIS Elements Software (Nikon) was used to find the central focal plane
487 in the GFP or mCherry channel of the ribosomal markers using single band pass filters. For all experiments,
488 the temperature was maintained at 25 °C using an incubator encapsulating the entire microscope (life
489 imaging services).

490 ***Confocal imaging of RPL-22:mCherry foci***
491 In Fig. 2d, a Nikon CREST X-light spinning disk confocal microscope was used to image L1 animals
492 immobilized on agarose pads by 10mM Levamisole and a coverslip. Animals were imaged at hatch or after
493 24h starvation. A 100x 1.45NA oil immersion objective was used to capture Z-stacks around manually set
494 focus plane with a single band pass filters for mCherry and GFP using 200ms exposure. Images were
495 deconvoluted using Huygens software.

496 ***Detection of animals and animal fluorescence in agar chambers***
497 A Matlab script was used to process raw images as described [34]. Sobel algorithm using the edge function
498 of Matlab (R2022b) was used to segment the animals from raw fluorescent images. Detected outline
499 endpoints closest to each other were connected to close gaps in the animal outline. From the outline a
500 binary mask was created to separate animals from background. For L1 starvation experiments in Fig. 1 and
501 Fig. S1 a U-net [63] network was trained to segment the binary mask of animals from raw brightfield images.
502 Segmentation was performed in brightfield channel to allow for the segmentation of non-fluorescent N2
503 control animals. The Sobel-based masks were used as the U-net training data. For both methods animal
504 fluorescence was measured from the area covered by the mask in the fluorescent channel. For Fig. 1h-I,
505 N2 animals were imaged in parallel and their auto fluorescent signal was subtracted from all measurements
506 due to the comparatively weak fluorescence signal of LMN-1:GFP. For Figs. 2a and 3d, only the background
507 signal from agar or bacteria was subtracted, as the tissue autofluorescence was negligible compared to the
508 fluorescence of RPL-29:GFP (Fig. S5e).

509 The masks were computationally straightened using a custom made Matlab function [34]. Straightened masks
510 were classified as either 'egg', 'worm' or 'error' using a decision tree-based classifier that was trained on a
511 small subset of manually annotated masks. The classifier was an ensemble of 20 bootstrap aggregation
512 decision trees (TreeBagger function of Matlab) that was trained on features length, standard deviation of
513 width, cv of width, maximal width, median width, maximal width/median width, volume, volume/length,
514 and entropy of width [34]. All experiments were classified with the same classifier, except for experiments
515 with autophagy deficient animals, whose occasionally irregular outline necessitated training of a separate
516 classifier for reliable error detection. Values derived from images with errors or missing animals were
517 excluded from further analyses.

518 ***Computation of volume and growth rate***
519 The volume of the animals in agarose chambers was derived from the straightened binary image masks
520 assuming rotational symmetry [35]. For growing animals, larval stage transitions were determined based on
521 the timing of the maximum of the second time derivative of the logarithm of animal volume. Using a
522 graphical user interface created in Matlab [34], the ecdysis timings were corrected manually based on
523 plateaus in animal growth curves caused prior to ecdysis. To minimize measurement error, for Fig. 3d and
524 Fig. S3a,b, the fluorescence and volume at t0 was estimated by fitting a linear model to the first 20
525 timepoints and the predicted value at t0 was plotted. Individuals for which less than 6 data points were
526 available in the first 20 timepoints were excluded. For Fig. 3c, the volume measurement was scaled to the
527 larval development by linearly interpolating the volume at 100 points per larval stage. The interpolated
528 values are plotted over the mean larval stage duration, such that the beginning and end of each larval stage
529 are aligned on the x-axis. The same scaling was used for fluorescence in Fig. S3c.

530 The rate of growth during starvation recovery for Fig. 4e-f was calculated in Matlab by smoothing every
531 individual animal's volume with the fit function's smoothing spline option using a smoothing parameter of
532 0.0001. Fits were manually inspected to ensure that the resulting volume interpolations are appropriate,

after which volume was interpolated at a time resolution of 1 minute. Volume growth rate by minute was calculated as the local slope of the smoothed volume curve by using gradient function. Individuals' growth rates were normalized to the mean growth rate of the control condition, and a mean of normalized growth rates was determined for every replicate chamber array.

Photobleaching based detection of GFP synthesis

L1 larvae starved for 16h in agarose chambers were imaged hourly for three hours before exposure to a 477nm laser (Celesta light engine, Lumencor) for 8 seconds at 100% laser power until approximately 60% of GFP signal had been bleached. Viability was not affected based on motility. Animals were subsequently imaged for 20 hours, the auto-fluorescence was subtracted using N2 animals as control, and the fluorescence signal was normalized by the first timepoint after photobleaching (Fig. S5b-c).

Data analysis: The net change in total fluorescence of GFP (g) is the difference in its production with rate p and degradation with rate constant d, such that:

$$\dot{g} = p - d * g \qquad \text{and} \qquad \frac{\dot{g}}{g} = \frac{p}{g} - d$$

Thus, for p > 0, the relative rate of change in GFP ($\frac{\dot{g}}{g}$) would increase after photobleaching, assuming that the rate constant d is unaffected by photobleaching. Conversely, if $\frac{\dot{g}}{g}$ is unaffected by photobleaching (as observed in Fig. S5b,d), p must be negligible.

Starvation recovery and survival assays

The ability of animals to recover growth after starvation (Fig. 4g) was measured daily at 25 °C by placing a total of 50-150 starving L1 larvae onto the bacterial lawn of fresh NGM plates from 3 independent cultures and counted immediately. After 2 or 3 days of growth (for shorter and longer than 4 day-starvation, respectively) animals that had exited L1 (based on their larger size) were considered to have resumed development and recovered from starvation.

Starvation survival (Fig. 4h) was determined by placing a minimum of 36 eggs per strain into agarose chambers without food and imaging every 17 min for 3 weeks at 25 °C. Worms were computationally detected as described above. Time of death was determined as the time of permanent loss of motility that was followed by death associated swelling (Fig. S2d).

Population Growth Model

Population growth for different tradeoff strategies was computed using numerical simulations in Matlab(R2022a) by calculating the relative fraction of animals among different strategies after different times of starvation during one generation. Survival s after time t of starvation was described by a Hill function with Hill coefficient n=4 and half-point σ.

$$s(t) = \frac{1}{1 + (t/\sigma)^4}$$

The lag time τ was determined by a linear relation τ = δ * t, where δ is the additional lag time per time of starvation. The tradeoff was model by the linear coupling $\sigma = k * \delta$. Parameter k was set to 56 days. 20 strains with δ being linearly spaced between 0.01 and 0.15 were computationally competed against each other, starting with a uniformly distributed population. This parameter range corresponds to a median survival σ spanning between 1.5 days and 22 days, and a lag times τ after 7 days of starvation between 1.7

hours and 25 hours, centered around the experimentally observed values shown in Fig. 3. Reproduction was kept equal among all strains, starting after 40 hours plus the respective lag time τ at a constant reproduction rate of 6 progeny per hour for 48 hours. The population was allowed to grow until it multiplied 20 times to simulate food exhaustion. The data shown in Fig. 4i is the relative frequency of each strain in the entire population at the end of the first starvation/recovery cycle.

Statistics

A robust one-way ANOVA (Fig. 1e-f) or a robust two-way ANOVA (Fig. 4d) (t1way and t2way from R package WRS2(v.1.1-4)) was performed to evaluate effects of genotype and protein group on the rate of change in LFQ fraction sizes (Table S3). For group-wise comparisons, Scheffe post-hoc test for one-way ANOVA and Games-Howel post-hoc test for two-way ANOVA was performed (Table S4). See Table S5 for testing statistical assumptions. Where appropriate, normal one- and two-way ANOVA, Kruskal-Wallis, Tukey's HSD, Dunn, and Tukey's HSD with Games-Howel modification tests are also reported (Table S3, Table S4). For LFQ group difference to zero in Figures 1e-f and 4d, a Benjamini-Hochberg multiple comparison adjusted Wilcox signed rank test was used. Bonferroni and Holm-Bonferroni adjustments are also reported (Table S6).

For Fig. 2c, Fig. S2f, and Fig. S6i-j a Benjamini-Hochberg multiple comparison adjusted two-sample t-test was performed (Table S1, Bonferroni and Holm-Bonferroni corrections are also reported).

588 **References**

589 1. Stearns, S. C. *The Evolution of Life Histories*. vol. 249 (Oxford University Press Oxford, 1992).
590 2. Mangel, M. & Stamps, J. Trade-offs between growth and mortality and the maintenance of individual
591 variation in growth. *Evol. Ecol. Res.* **3**, (2001).
592 3. Rion, S. & Kawecki, T. J. Evolutionary biology of starvation resistance: what we have learned from
593 Drosophila. *J. Evol. Biol.* **20**, 1655–1664 (2007).
594 4. Bergkessel, M., Basta, D. W. & Newman, D. K. The physiology of growth arrest: uniting molecular and
595 environmental microbiology. *Nat. Rev. Microbiol.* **14**, 549–562 (2016).
596 5. Abram, F., Arcari, T., Guerreiro, D. & O'Byrne, C. P. Chapter Four - Evolutionary trade-offs between
597 growth and survival: The delicate balance between reproductive success and longevity in bacteria. in
598 *Advances in Microbial Physiology* (eds. Poole, R. K. & Kelly, D. J.) vol. 79 133–162 (Academic Press,
599 2021).
600 6. Shoval, O. *et al.* Evolutionary Trade-Offs, Pareto Optimality, and the Geometry of Phenotype Space.
601 *Science* **336**, 1157–1160 (2012).
602 7. Yang, Y. *et al.* Temporal scaling of aging as an adaptive strategy of *Escherichia coli*. *Sci. Adv.* **5**,
603 eaaw2069 (2019).
604 8. Biselli, E., Schink, S. J. & Gerland, U. Slower growth of Escherichia coli leads to longer survival in
605 carbon starvation due to a decrease in the maintenance rate. *Mol. Syst. Biol.* **16**, e9478 (2020).
606 9. Basan, M. Resource allocation and metabolism: the search for governing principles. *Curr. Opin.*
607 *Microbiol.* **45**, 77–83 (2018).
608 10. Basan, M. *et al.* A universal trade-off between growth and lag in fluctuating environments. *Nature*
609 **584**, 470–474 (2020).
610 11. Scott, M. & Hwa, T. Bacterial growth laws and their applications. *Curr. Opin. Biotechnol.* **22**, 559–65
611 (2011).
612 12. Schaechter, M., MaalØe, O. & Kjeldgaard, N. O. Dependency on Medium and Temperature of Cell Size
613 and Chemical Composition during Balanced Growth of *Salmonella typhimurium*. *Microbiology* **19**,
614 592–606 (1958).
615 13. Dmitriew, C. M. The evolution of growth trajectories: what limits growth rate? *Biol. Rev.* **86**, 97–116
616 (2011).
617 14. Liebermeister, W. *et al.* Visual account of protein investment in cellular functions. *Proc. Natl. Acad.*
618 *Sci.* **111**, 8488–8493 (2014).
619 15. Baugh, L. R. & Hu, P. J. Starvation Responses Throughout the *Caenorhabditis elegans* Life Cycle.
620 *Genetics* **216**, 837–878 (2020).
621 16. Kaur, J. & Debnath, J. Autophagy at the crossroads of catabolism and anabolism. *Nat. Rev. Mol. Cell*
622 *Biol.* **16**, 461–472 (2015).
623 17. Kang, C., You, Y. & Avery, L. Dual roles of autophagy in the survival of Caenorhabditis elegans during
624 starvation. *Genes Dev.* **21**, 2161–2171 (2007).
625 18. Kraft, C., Deplazes, A., Sohrmann, M. & Peter, M. Mature ribosomes are selectively degraded upon
626 starvation by an autophagy pathway requiring the Ubp3p/Bre5p ubiquitin protease. *Nat. Cell Biol.*
627 **10**, 602–610 (2008).
628 19. An, H. & Harper, J. W. Systematic analysis of ribophagy in human cells reveals bystander flux during
629 selective autophagy. *Nat. Cell Biol.* **20**, 135–143 (2018).
630 20. An, H., Ordureau, A., Körner, M., Paulo, J. A. & Harper, J. W. Systematic quantitative analysis of
631 ribosome inventory during nutrient stress. *Nature* **583**, 303–309 (2020).

632 21. Wyant, G. A. *et al.* NUFIP1 is a ribosome receptor for starvation-induced ribophagy. *Science* **360**,
633 751–758 (2018).
634 22. Gretzmeier, C. *et al.* Degradation of protein translation machinery by amino acid starvation-induced
635 macroautophagy. *Autophagy* **13**, 1064–1075 (2017).
636 23. López, A. R. *et al.* Autophagy-mediated control of ribosome homeostasis in oncogene-induced
637 senescence. *Cell Rep.* **42**, 113381 (2023).
638 24. Beese, C. J., Brynjólfsdóttir, S. H. & Frankel, L. B. Selective Autophagy of the Protein Homeostasis
639 Machinery: Ribophagy, Proteaphagy and ER-Phagy. *Front. Cell Dev. Biol.* **0**, (2020).
640 25. Schulenburg, H. & Félix, M.-A. The Natural Biotic Environment of *Caenorhabditis elegans*. *Genetics*
641 **206**, 55–86 (2017).
642 26. Arike, L. *et al.* Comparison and applications of label-free absolute proteome quantification methods
643 on Escherichia coli. *J. Proteomics* **75**, 5437–5448 (2012).
644 27. Schwanhäusser, B. *et al.* Global quantification of mammalian gene expression control. *Nature* **473**,
645 337–342 (2011).
646 28. Cox, J. *et al.* Accurate Proteome-wide Label-free Quantification by Delayed Normalization and
647 Maximal Peptide Ratio Extraction, Termed MaxLFQ. *Mol. Cell. Proteomics MCP* **13**, 2513–2526
648 (2014).
649 29. Hibshman, J. D. *et al.* Nonselective autophagy reduces mitochondrial content during starvation in
650 Caenorhabditis elegans. *Am. J. Physiol. - Cell Physiol.* **315**, C781–C792 (2018).
651 30. Perez, M. F. & Lehner, B. Vitellogenins - Yolk Gene Function and Regulation in Caenorhabditis elegans.
652 *Front. Physiol.* **10**, 1067 (2019).
653 31. Schwinn, M. K. *et al.* CRISPR-Mediated Tagging of Endogenous Proteins with a Luminescent Peptide.
654 *ACS Chem. Biol.* **13**, 467–474 (2018).
655 32. Sands, B. *et al.* A toolkit for DNA assembly, genome engineering and multicolor imaging for C.
656 elegans. *Transl. Med. Aging* **2**, 1–10 (2018).
657 33. Liu, J. *et al.* Essential Roles for Caenorhabditis elegans Lamin Gene in Nuclear Organization, Cell
658 Cycle Progression, and Spatial Organization of Nuclear Pore Complexes. *Mol. Biol. Cell* **11**, 3937–
659 3947 (2000).
660 34. Stojanovski, K., Großhans, H. & Towbin, B. D. Coupling of growth rate and developmental tempo
661 reduces body size heterogeneity in C. elegans. *Nat. Commun.* **13**, 3132 (2022).
662 35. Moore, B. T., Jordan, J. M. & Baugh, L. R. WormSizer: High-throughput Analysis of Nematode Size and
663 Shape. *PLOS ONE* **8**, e57142 (2013).
664 36. Takacs, Z. *et al.* ATG-18 and EPG-6 are Both Required for Autophagy but Differentially Contribute to
665 Lifespan Control in Caenorhabditis elegans. *Cells* **8**, 236 (2019).
666 37. Stroustrup, N. *et al.* The Caenorhabditis elegans Lifespan Machine. *Nat. Methods* **10**, 665–670
667 (2013).
668 38. Rennick, J. J., Nowell, C. J., Pouton, C. W. & Johnston, A. P. R. Resolving subcellular pH with a
669 quantitative fluorescent lifetime biosensor. *Nat. Commun.* **13**, 6023 (2022).
670 39. Kneen, M., Farinas, J., Li, Y. & Verkman, A. S. Green Fluorescent Protein as a Noninvasive Intracellular
671 pH Indicator. *Biophys. J.* **74**, 1591–1599 (1998).
672 40. Pankiv, S. *et al.* p62/SQSTM1 Binds Directly to Atg8/LC3 to Facilitate Degradation of Ubiquitinated
673 Protein Aggregates by Autophagy*. *J. Biol. Chem.* **282**, 24131–24145 (2007).
674 41. Kostich, M., Fire, A. & Fambrough, D. M. Identification and molecular-genetic characterization of a
675 LAMP/CD68-like protein from Caenorhabditis elegans. *J. Cell Sci.* **113**, 2595–2606 (2000).

676 42. Uppaluri, S. & Brangwynne, C. P. A size threshold governs Caenorhabditis elegans developmental
677 progression. *Proc. Biol. Sci.* **282**, 20151283 (2015).
678 43. Olmedo, M. *et al.* Prolonged quiescence delays somatic stem cell-like divisions in Caenorhabditis
679 elegans and is controlled by insulin signaling. *Aging Cell* **19**, e13085 (2020).
680 44. Gollwitzer, P., Grützmacher, N., Wilhelm, S., Kümmel, D. & Demetriades, C. A Rag GTPase dimer code
681 defines the regulation of mTORC1 by amino acids. *Nat. Cell Biol.* **24**, 1394–1406 (2022).
682 45. Al-Refaie, N. *et al. An mTOR/RNA Pol I Axis Shapes Chromatin Architecture in Response to Fasting*.
683 http://biorxiv.org/lookup/doi/10.1101/2023.07.22.550032 (2023) doi:10.1101/2023.07.22.550032.
684 46. Saxton, R. A. & Sabatini, D. M. mTOR Signaling in Growth, Metabolism, and Disease. *Cell* **168**, 960–
685 976 (2017).
686 47. Eden, E. *et al.* Proteome Half-Life Dynamics in Living Human Cells. *Science* **331**, 764–768 (2011).
687 48. de la Calle Arregui, C. *et al.* Limited survival and impaired hepatic fasting metabolism in mice with
688 constitutive Rag GTPase signaling. *Nat. Commun.* **12**, 3660 (2021).
689 49. Gurvich, Y., Leshkowitz, D. & Barkai, N. Dual role of starvation signaling in promoting growth and
690 recovery. *PLoS Biol.* **15**, e2002039 (2017).
691 50. Scharf, I., Filin, I. & Ovadia, O. A trade-off between growth and starvation endurance in a pit-building
692 antlion. *Oecologia* **160**, 453–460 (2009).
693 51. Stamps, J. A. Growth-mortality tradeoffs and 'personality traits' in animals. *Ecol. Lett.* **10**, 355–363
694 (2007).
695 52. Roux, A. E., Langhans, K., Huynh, W. & Kenyon, C. Reversible Age-Related Phenotypes Induced during
696 Larval Quiescence in C. elegans. *Cell Metab.* **23**, 1113–1126 (2016).
697 53. Birgisdottir, Å. B., Lamark, T. & Johansen, T. The LIR motif – crucial for selective autophagy. *J. Cell Sci.*
698 **126**, 3237–3247 (2013).
699 54. Korem Kohanim, Y. *et al.* A Bacterial Growth Law out of Steady State. *Cell Rep.* **23**, 2891–2900 (2018).
700 55. Erickson, D. W. *et al.* A global resource allocation strategy governs growth transition kinetics of
701 Escherichia coli. *Nature* **551**, 119 (2017).
702 56. Steffen, K. K. & Dillin, A. A Ribosomal Perspective on Proteostasis and Aging. *Cell Metab.* **23**, 1004–
703 1012 (2016).
704 57. Large-Scale Screening for Targeted Knockouts in the Caenorhabditis elegans Genome. *G3*
705 *GenesGenomesGenetics* **2**, 1415–1425 (2012).
706 58. Meeuse, M. W. *et al.* Developmental function and state transitions of a gene expression oscillator in
707 Caenorhabditis elegans. *Mol. Syst. Biol.* **16**, e9498 (2020).
708 59. Hills-Muckey, K. *et al.* An engineered, orthogonal auxin analog/AtTIR1(F79G) pairing improves both
709 specificity and efficacy of the auxin degradation system in Caenorhabditis elegans. *Genetics* **220**,
710 iyab174 (2021).
711 60. Cox, J. & Mann, M. MaxQuant enables high peptide identification rates, individualized p.p.b.-range
712 mass accuracies and proteome-wide protein quantification. *Nat. Biotechnol.* **26**, 1367–1372 (2008).
713 61. Tyanova, S. *et al.* The Perseus computational platform for comprehensive analysis of (prote)omics
714 data. *Nat. Methods* **13**, 731–740 (2016).
715 62. Turek, M., Besseling, J. & Bringmann, H. Agarose Microchambers for Long-term Calcium Imaging of
716 Caenorhabditis elegans. *JoVE J. Vis. Exp.* e52742 (2015) doi:10.3791/52742.
717 63. Ronneberger, O., Fischer, P. & Brox, T. U-Net: Convolutional Networks for Biomedical Image
718 Segmentation. Preprint at https://doi.org/10.48550/arXiv.1505.04597 (2015).
719 64. Perez-Riverol, Y. *et al.* The PRIDE database resources in 2022: a hub for mass spectrometry-based
720 proteomics evidences. *Nucleic Acids Res.* **50**, D543–D552 (2021).

Acknowledgements

We thank Sebastian Leidel, Anat Bren, Peter Lenart, and Helge Grosshans for helpful feedback on the manuscript. We acknowledge support by the Microscopy Imaging Center at the University of Bern. Some strains were provided by the CGC, which is funded by NIH Office of Research Infrastructure Programs (P40 OD010440). Figures 1a-c and 3a were created with BioRender.com. Alleles *xe232, syb3768*, *syb1945*, *syb1880* and *syb1903* were created by SunnyBiotech.

Funding

This work received support from an SNSF Eccellenza Grant (PCEFP3_181204) to BDT and the Bern Research Foundation (34/2022).

Author contributions

BDT and JT conceived the study, wrote the manuscript. JD, NS, BDT and JT edited the manuscript. JD and DSS conducted mass spectrometry measurements. JT and JP conducted all other experiments. JT and BDT performed computational and statistical analyses. BDT performed fitness modeling. SP implemented the U-net based image segmentation. NS designed alleles *syb1945*, *syb1880* and *syb1903*. JT, NS and JP created and validated strains used in the study.

Competing interests

The authors declare no competing interest.

Data and Code availability

The mass spectrometry proteomics data have been deposited to the ProteomeXchange Consortium via the PRIDE[64] partner repository with the dataset identifier PXD050951. Volume and fluorescence data from microscopy experiments is available in supplemental tables. Raw images are available upon request from the authors. Code for image analysis was as used in[34] (10.5281/zenodo.10032867). Code for the population growth model is available as supplementary information.

Supplementary Materials

Figs. S1 to S7

Tables S1 to S6